Boundary-Layer Meteorol
DOI 10.1007/s10546-011-9613-5

ARTICLE

Coherent Structures and the Dissimilarity of Turbulent Transport of Momentum and Scalars in the Unstable Atmospheric Surface Layer

Dan Li · Elie Bou-Zeid

Received: 23 September 2010 / Accepted: 30 March 2011
© Springer Science+Business Media B.V. 2011

Abstract Atmospheric stability effects on the dissimilarity between the turbulent transport of momentum and scalars (water vapour and temperature) are investigated in the neutral and unstable atmospheric surface layers over a lake and a vineyard. A decorrelation of the momentum and scalar fluxes is observed with increasing instability. Moreover, different measures of transport efficiency (correlation coefficients, efficiencies based on quadrant analysis and bulk transfer coefficients) indicate that, under close to neutral conditions, momentum and scalars are transported similarly whereas, as the instability of the atmosphere increases, scalars are transported increasingly more efficiently than momentum. This dissimilarity between the turbulent transport of momentum and scalars under unstable conditions concurs with, and is likely caused by, a change in the topology of turbulent coherent structures. Previous laboratory and field studies report that under neutral conditions hairpin vortices and hairpin packets are present and dominate the vertical fluxes, while under free-convection conditions thermal plumes are expected. Our results (cross-stream vorticity variation, quadrant analysis and time series analysis) are in very good agreement with this picture and confirm a change in the structure of the coherent turbulent motions under increasing instability, although the exact structure of these motions and how they are modified by stability requires further investigation based on three-dimensional flow data.

Keywords Coherent structures · Hairpin vortices · Quadrant analysis · Reynolds analogy · Thermal plumes · Transport efficiencies

1 Introduction

The turbulent transport of momentum and scalars has been the subject of active research in many disciplines such as fluid mechanics, boundary-layer meteorology, eco-hydrology and

D. Li · E. Bou-Zeid (✉)
Department of Civil and Environmental Engineering, Princeton University,
E-Quad, Princeton, NJ 08544, USA
e-mail: ebouzeid@princeton.edu

Published online: 28 April 2011

air quality. It has long been assumed that turbulence transports all scalars such as temperature, water vapour and trace gases similarly (the Lewis analogy for turbulence, Kays et al. 2005). This analogy is often extended to include momentum and referred to as the Reynolds analogy. The Reynolds analogy has important applications in turbulent flow simulations, parametrizations and measurements; but it is recognized that this analogy is generally invalid. In the atmospheric boundary layer (ABL), the Reynolds analogy is considered to be applicable only under neutral conditions. As the role of buoyancy increases, the flux–profile relationships (Brutsaert 2005) and the transport efficiencies (De Bruin et al. 1993; Choi et al. 2004; Bou-Zeid et al. 2010) for momentum and scalars become increasingly different. The need to understand the physical causes of this dissimilarity and the role of atmospheric stability in the failure of the Reynolds analogy motivates this study.

Previous studies revealed a number of reasons for dissimilarity among scalars in the ABL such as advection (Lee et al. 2004; Assouline et al. 2008); unsteadiness (McNaughton and Laubach 1998); entrainment at the top of the ABL (Mahrt 1991a; Sempreviva and Hojstrup 1998; De Bruin et al. 1999; Sempreviva and Gryning 2000; Asanuma et al. 2007; Katul et al. 2008; Cava et al. 2008) and differences in sources and sinks (Moriwaki and Kanda 2006; Williams et al. 2007; Detto et al. 2008; Moene and Schuttemeyer 2008). The dissimilar transport of momentum and scalars, on the other hand, has been linked to the canopy effect (Katul et al. 1997a). Though our focus here is on the effect of atmospheric stability on the dissimilar transport of momentum and scalars, not among scalars, we note that these non-local effects could also potentially play a role in momentum–scalar flux dissimilarity.

If atmospheric stability is found to play a role in momentum and scalar flux dissimilarity (as expected), then one physical explanation would be the one related to turbulent coherent structures and how they are modified by buoyancy. These structures are of interest because they have been shown to be responsible for a large fraction of the transport of momentum and scalars (Robinson 1991; Marusic et al. 2010a), leading to a paradigm shift in the studies of turbulent transport in the atmosphere, which is no longer viewed as resulting from random turbulent fluctuations across a velocity or scalar gradient. Many laboratory and numerical studies revealed that various forms of coherent structures such as low-speed streaks, hairpin vortices and large-scale motions exist in pipe flows, channel flows and turbulent boundary layers (e.g. Kline et al. 1967; Head and Bandyopadhyay 1981; Kim and Adrian 1999; Monty et al. 2007; Ringuette et al. 2008; Marusic et al. 2010a). It is now generally recognized that hairpin vortices (first proposed by Theodorsen 1952) and the streamwise packets they form are the primary coherent structures forming in the logarithmic layer of the neutral turbulent boundary layer under laboratory conditions (Adrian 2007). Coherent structures have been also investigated in the ABL through numerical simulations, scale model experiments, and field experiments (e.g. Hommema and Adrian 2003; Carper and Porte-Agel 2004; Kanda 2006; Huang et al. 2009; Inagaki and Kanda 2010; Horiguchi et al. 2010). Such investigations, focusing mainly on the neutral ABL, found turbulent structures similar to laboratory structures, such as hairpins, hairpin packets and cross-stream vortices (which might be the leading edges of hairpin vortices) and large-scale organized motions (e.g. Boppe et al. 1999; Horiguchi et al. 2010). In addition, recent review articles have compiled studies that indicate that turbulence and the pressure field in the atmospheric surface layer (ASL) scale similarly to canonical wall-bounded flows (Marusic et al. 2010a), further suggesting that the coherent structures responsible for this scaling are similar. Thus, despite studies suggesting that detached eddies from the outer layer can intrude and be active (i.e. produce fluxes and not only contribute to variances) in the surface layer of the high Reynolds number ABL (Hunt and Morrison 2000; Hunt and Carlotti 2001; Hogstrom et al. 2002; McNaughton and Brunet 2002; Drobinski et al. 2004; Smedman et al. 2007; Drobinski et al. 2007), the classic and more

prevalent view of surface-layer turbulence postulates that active structures mainly emerge at the surface and then grow from there, similar to laboratory wall-bounded flows.

Nevertheless, these atmospheric coherent structures must differ from the laboratory-observed structures since in the ABL they can be modulated by the surface buoyancy flux under statically stable or unstable conditions. Under unstable conditions, turbulence is shaped by the relative magnitude of buoyancy and shear productions of turbulent kinetic energy and in the limit of free convection would be expected to resemble Rayleigh-Bénard convection (Schmidt and Schumann 1989) rather than wall-bounded turbulence. Under such unstable conditions, ramp structures in the time series of scalar quantities, such as temperature, water vapour and CO_2 concentrations are often interpreted as signatures of thermal plumes (Stull 1988). In the slightly unstable ABL, large-scale horizontal roll vortices form, and have usually been attributed to the combined buoyant and shear effects (Mason and Sykes 1980; Etling and Brown 1993; Boppe et al. 1999), though such large-scale rolls are now known to exist (and to meander) even in neutral laboratory flows (Hutchins and Marusic 2007). This evidence indicates that atmospheric stability effects shape and modify turbulence structure in the ABL (Mason and Sykes 1980, 1982; Wyngaard 1985; Boppe et al. 1999). More concretely, for the transition from a neutral to an unstable surface layer, Hommema and Adrian (2003), using smoke visualizations, found clear evidence of hairpin packets under neutral conditions with inclination angles similar to those observed in laboratory studies. They also observed that, under moderately unstable conditions, the individual hairpins lifted off the surface, leading to an increase in the inclination angle of the packets (same observations also made by Carper and Porte-Agel 2004). Under highly unstable conditions, nevertheless, Hommema and Adrian (2003) could not detect any hairpins but their visualizations clearly depict upward-moving thermal plumes. However, the implications of such modification for the similarity, or lack thereof, of the transport of momentum and scalars over the full range of stabilities, are still elusive.

To quantify the effect of stability on transport similarity and the link to coherent structure modulation by buoyancy, we rely significantly herein on quadrant analysis. Previous studies reported that the characteristics (e.g. time fraction, flux contribution, etc.) of ejections and sweeps, which are the primary constitutive eddy motions of coherent structures associated with momentum and scalar fluxes, differ in the canopy sublayer, roughness sublayer, and ASL (see Katul et al. 1997b for a review). However, less is known about the atmospheric stability effects on ejections and sweeps in the ASL and how the changes of their characteristics are different for momentum and scalar fluxes.

The objective of this study is thus to investigate the dissimilar transport of momentum and scalars in the ABL, the role of atmospheric stability in this dissimilarity, and whether it can be linked to modifications of the coherent structures in the ASL under different stabilities. This article is organized in the following way: Sect. 2 describes the experimental set-up and data processing, followed by a brief introduction of quadrant analysis and transport efficiencies in Sect. 3; in Sect. 4, the results are presented and discussed. Section 5 presents a summary and the conclusions.

2 Experimental Set-Up and Data Processing

The major experimental dataset used here is from the Lake-Atmosphere Turbulent EXchanges (LATEX) study performed over Lac Leman, Switzerland, during the summer of 2006. Full details of the experiment can be found in Vercauteren et al. (2008) and Bou-Zeid et al. (2008). The main deployed instruments of relevance to our study include four three-dimensional sonic

Fig. 1 Set-up of the two eddy-covariance stations over the vineyard (downstream view from station 1 on *left*, upstream view from station 1 on *right*)

anemometers (Campbell Scientific CSAT3) and four open-path gas analyzers (LICOR-7500) measuring wind velocity, air temperature and water vapour concentration at four heights above the water surface (1.65, 2.30, 2.95 and 3.60 m) from mid August to late October in 2006 (day-of-year 226–298). Other instruments included various sensors measuring air and water temperatures and net radiation. Data quality control procedures and the validation and verification of the analysis are similar to Vercauteren et al. (2008) who showed that waves during the experiment are wind driven with very rare swell events and are too low to affect the atmospheric flow at the measurement height (they simply act as surface roughness elements). Only winds from directions facing the sonic tower and flowing over a large uninterrupted fetch of surface lake water (about 10 km) are used.

The vineyard dataset consisted of two pairs of sonic anemometers/gas analyzers mounted on two different towers (about 100 m apart). The sensors (a Campbell scientific CSAT3 and a LICOR LI7500 on each tower) were set-up at a height of 2.4 m in the middle and at the edge of a vineyard (Fig. 1) near Geneva, Switzerland. As can be seen in the figure, the stations are in heterogeneous terrain with a moderate slope upwind. The dataset was intentionally selected in such non-ideal conditions that are strikingly different from the lake conditions because, if the observations from the lake experiment (homogeneous, flat, and ideal surface) are also confirmed by the vineyard dataset, the robustness of the findings would be more significant.

The raw data in both experiments were collected at 20 Hz, and we use 15-min averaging to define Reynolds means and fluctuations. Data pre-processing mainly involves yaw and pitch corrections of the sonic anemometer velocities, linear detrending and the Webb correction applied to fluxes.

Friction velocity u_* is calculated following $u_* = (\overline{u'w'}^2 + \overline{v'w'}^2)^{1/4}$ and sensible and latent heat fluxes are calculated using the eddy-covariance method:

$$H = \rho C_\mathrm{p} \overline{w'T'}, \tag{1}$$

$$E = \rho L_\mathrm{v} \overline{w'q'}, \tag{2}$$

where, u, v and w are the streamwise, cross-stream and vertical velocities, respectively; T is the temperature; and q is the specific humidity. The temperature is corrected for the effect of humidity on sonic-measured temperatures, but no conversion to potential temperature is needed since the instruments are very close to each other and to the surface. The prime denotes

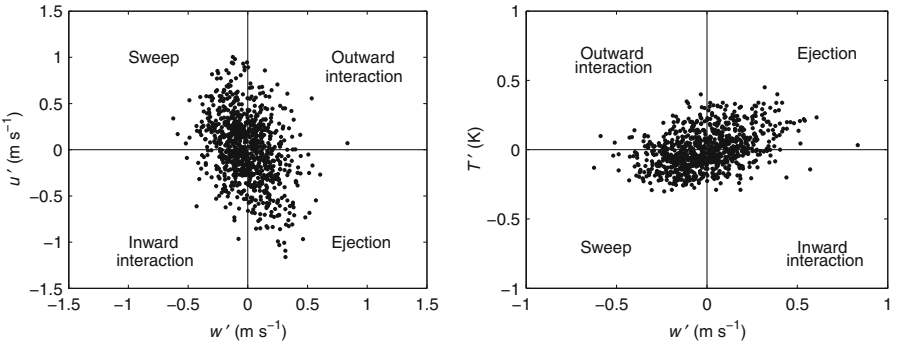

Fig. 2 Definitions of quadrants for momentum and scalar fluxes (heat flux illustrated here)

the turbulent fluctuations relative to the Reynolds average, which is denoted by the overbar. ρ, C_p and L_v are the air density, the specific heat capacity at constant pressure and the latent heat of vaporization of water, respectively. The Obukhov length scale, L, is calculated using the following relationship:

$$L = -\frac{\bar{T}u_*^3}{\kappa g\left(\overline{w'T'} + 0.61\bar{T}\overline{w'q'}\right)}, \tag{3}$$

where κ is the von Karman constant (0.4) and g is the gravitational acceleration.

For this study, only data collected under unstable conditions were analyzed, and the data were selected based on the following criteria:

(1) the turbulence intensity must be less than 0.5 to justify the use of Taylor's hypothesis;
(2) the variance of the velocity, temperature and water vapour concentration for each 15-min record must be five times larger than the root-mean-square (r.m.s.) noise (as specified by the manufacturer) of the corresponding instrument to ensure that the signal-to-noise ratio is sufficiently high; this is especially important for the computation of higher-order moments;
(3) the momentum and scalar fluxes must be larger than a threshold: $u_* > 0.01\,\mathrm{m\,s^{-1}}$, $H > 10\,\mathrm{W\,m^{-2}}$ and $L_\mathrm{v}E > 10\,\mathrm{W\,m^{-2}}$, again to ensure that the fluxes are well resolved by the instruments and that the trends in the transport efficiency variations are not due to vanishing fluxes.

3 Methodology

3.1 Quadrant Analysis

The definition of each quadrant in our analysis follows Shaw et al. (1983) and Katul et al. (1997a,b) for momentum and scalar fluxes, respectively, as shown in Fig. 2.

The flux contribution of each quadrant is defined as

$$S(i) = \frac{\overline{w'c'}_i}{\overline{w'c'}}, \tag{4}$$

$$\overline{w'c'}_i = \frac{1}{t_\mathrm{p}} \int_0^{t_\mathrm{p}} \overline{w'c'} I_i(t) \mathrm{d}t, \tag{5}$$

where $c = u$, q *or* T, t_p is the time period over which Reynolds averaging is performed (15 min), and

$$I_i = \begin{cases} 1 & \text{if } w'c' \text{ is in quadrant } i \\ 0 & \text{otherwise.} \end{cases}$$

The fraction of time occupied by events from quadrant i can be computed as follows:

$$D(i) = \frac{1}{t_\mathrm{p}} \int_0^{t_\mathrm{p}} I_i(t) \mathrm{d}t. \tag{6}$$

3.2 Transport Efficiencies

The transport efficiencies for momentum, water vapour and heat are often defined as the correlation coefficients:

$$R_{wc} = \frac{\overline{w'c'}}{\sigma_w \sigma_c}, \tag{7}$$

where σ_w and σ_c are the standard deviations of vertical velocity and the parameter c over a 15-min interval, respectively. Based on quadrant analysis, another measure of transport efficiency can be defined as the ratio of the total flux divided by the flux that is transported downgradient:

$$\eta = \frac{F_\mathrm{total}}{F_\mathrm{downgradient}} = \frac{F_\mathrm{downgradient} + F_\mathrm{upgradient}}{F_\mathrm{downgradient}}. \tag{8}$$

Note that downgradient fluxes are transported by ejection and sweep events, thus the new transport efficiency is equal to

$$\eta = \frac{\overline{w'c'}}{\overline{w'c'}_\mathrm{ejections} + \overline{w'c'}_\mathrm{sweeps}}. \tag{9}$$

This measure of transport efficiency and its relationship with the correlation coefficient were discussed in Wyngaard and Moeng (1992); the two measures of transport efficiency are comparable when a joint Gaussian distribution is assumed.

4 Results and Discussions

4.1 Atmospheric Stability Effects on Transport Similarity

Atmospheric stability effects on the dissimilarity between the turbulent transport of momentum and scalar fluxes are investigated by analyzing the statistics, spectra and efficiencies associated with turbulent fluxes (e.g. $u'w'$, $w'q'$, $w'T'$, and so on). First, the correlation coefficients of the momentum flux and the two scalar fluxes are examined in Fig. 3. The correlation coefficients of momentum flux and two scalar fluxes are defined as

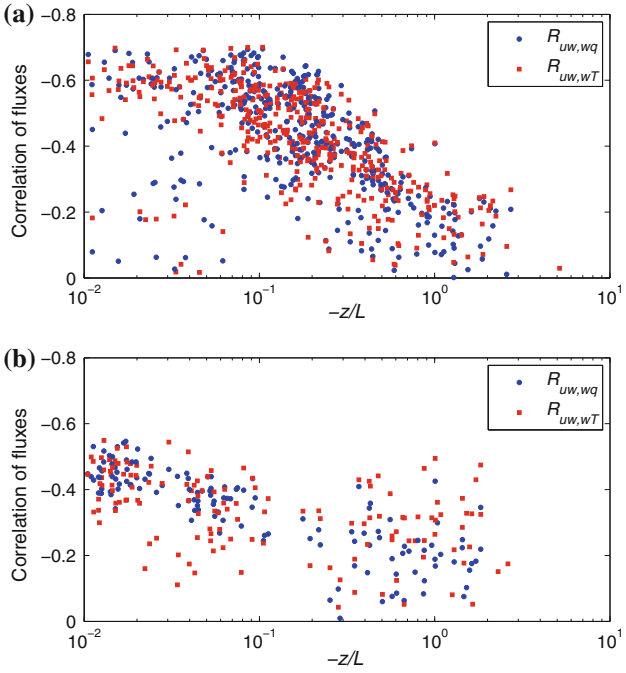

Fig. 3 Correlations of momentum and scalar fluxes. **a** Lake data and **b** vineyard data

$$R_{uw,wq} = \frac{\overline{\left(u'w' - \overline{u'w'}\right)\left(w'q' - \overline{w'q'}\right)}}{\sigma_{u'w'}\sigma_{w'q'}}, \tag{10}$$

$$R_{uw,wT} = \frac{\overline{\left(u'w' - \overline{u'w'}\right)\left(w'T' - \overline{w'T'}\right)}}{\sigma_{u'w'}\sigma_{w'T'}}, \tag{11}$$

where $\sigma_{u'w'}$, $\sigma_{w'q'}$ and $\sigma_{w'T'}$ are the standard deviations of $u'w'$, $w'q'$ and $w'T'$, respectively. Under near-neutral conditions, high correlations exist between momentum and scalar fluxes, which indicate that these fluxes are performed by the same motions in the ASL. As instability increases, the correlations between momentum and scalar fluxes diminish implying that they are now performed by different eddies or at different time periods during an event. Despite the higher scatter that might be due to surface inhomogeneity or canopy effects, the fact that the vineyard data give very similar qualitative trends indicates that the dissimilarity between the turbulent transport of momentum and scalar fluxes is controlled by atmospheric stability effects rather than the surface type in this analysis.

Spectral analysis is utilized to investigate the scale dependence of this dissimilarity between the turbulent transport of momentum and scalars. Two selected 2-h intervals, one under near-neutral and one under convective conditions, from the lake dataset were analyzed with each interval divided into 60 sub-segments (bins) of 2 min; the spectra computed for the 60 bins were subsequently averaged and plotted. The basic characteristics of the two selected intervals are presented in Table 1. We only report two periods because the trends will be difficult to observe if multiple spectra are reported since they will not exactly collapse. We stress, however, that we have verified that these two intervals are very representative of

Table 1 Characteristics of the two selected segments (Figs. 4, 5)

	Figures 4 and 5a	Figures 4 and 5b
z/L	−0.1252	−0.6244
R_{uq}	−0.4515	−0.2399
R_{uT}	−0.3980	−0.0108
R_{qT}	0.7008	0.8703
$R_{uw,wq}$	−0.5062	−0.2269
$R_{uw,wT}$	−0.4240	−0.0645
$R_{wq,wT}$	0.7426	0.9058

close-to-neutral (interval 1) versus unstable (interval 2) conditions: the dependence of the spectra we analyze on stability is therefore consistent.

Table 1 shows that the second interval (b) is under unstable conditions while the first interval (a) is under close-to-neutral conditions. Both segments have very high correlations between temperature (T) and humidity (q), with the two scalars slightly more correlated in the second interval. However, the second interval has much lower correlations between horizontal velocity (u) and scalars (q, T). The resulting lower correlations between momentum flux ($u'w'$) and scalar fluxes ($w'q'$, $w'T'$) indicate that at higher instability, events transporting momentum and scalars are distinct and dissimilarity in transport mechanisms and efficiencies is possible.

As can be seen from Figs. 4 and 5, the characteristics associated with the coherence and phase spectra (see Stull 1988 for definitions) of the two segments correspond to the correlations shown in Table 1. The higher coherence spectra (which can be understood as a frequency-dependent correlation coefficient) of u and q, T in Fig. 4a (both figures on the left) indicate that, under near-neutral conditions, the horizontal velocity and the scalars are better correlated, as are the momentum flux ($u'w'$) and scalar fluxes ($w'q'$, $w'T'$). While in Fig. 4b (both figures on the right), the coherence spectra of u and q, T, as well as the coherence spectra of the fluxes $u'w'$ and $w'q'$, $w'T'$, are considerably lower than those in Fig. 4a, implying separate or unsynchronized transport of momentum and scalar fluxes. Two features are to be noted: (1) the decrease in the coherence spectra affects all frequencies and scales; and (2) the coherence spectra of q and T and their vertical fluxes have very high values (not shown here) indicating very strong similarity in scalar transport in this dataset.

The underlying cause of the momentum/scalar transport dissimilarity is also investigated using the phase spectra (Fig. 5), which can be understood as a measure of the synchronization of the minima and maxima of the signals. A zero value implies perfect synchronization: minima of one signal tend to occur near minima or maxima of the other. More importantly, scattered values indicate very poor synchronization and a lack of correlation of the signals. Figure 5 shows that, at higher instability, the phase lags between momentum and scalar fluxes are more pronounced, very scattered, and start at large scales; in near-neutral conditions, however, the two are consistently in-phase for most of the low-frequency or large-scale ranges.

Mahrt (1991b) studied the correlation between horizontal and vertical velocity components in the heated boundary layer by means of wavelet analysis and found that a systematic phase difference between the two velocity components resulted in a decreasing Prandtl number with increasing instability, which is consistent with our results (see the approximate 50° phase lag between u and w in Fig. 5 under unstable conditions). It should also be pointed out

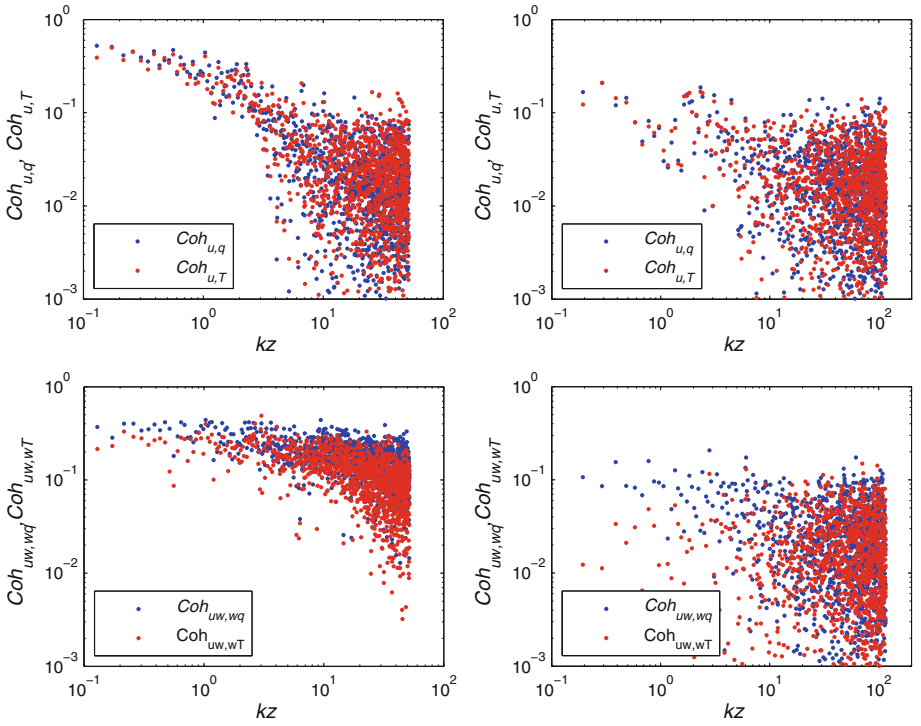

Fig. 4 Spectral analysis of two selected segments (coherence spectra). **a** $z/L = -0.1252$ and **b** $z/L = -0.6244$

that the observed large scatter at smaller scales (higher frequencies) under all stabilities is to be expected and this is because the energy and scalar variance cascade processes reduce the coherence of turbulent fluxes as the scales decrease, compared to the large scales where the correlations are high due to the well-correlated fluxes at the boundaries.

4.2 Atmospheric Stability Effects on Transport Efficiencies

Two measures of transport efficiency, correlation coefficients and the transport efficiencies based on quadrant analysis (Eqs. 7, 9), are examined to investigate whether the stability effects that we have illustrated on the correlations of turbulent fluxes are actually of significance in turbulence modelling. As shown in Figs. 6 and 7, it is quite clear that, while at neutral stability turbulence transports momentum and scalars with very similar efficiencies, when the buoyancy effects increase, the scalar transport efficiency increases while the momentum transport efficiency decreases sharply. In addition, except for the momentum transport efficiencies over the vineyard, which could be influenced by canopy effects and thus display considerable scatter, all the other efficiencies and their ratios seem to follow Monin–Obukhov Similarity Theory (MOST) scaling rather well. This supports the view that we introduced as the more generally accepted description of active ASL turbulence being produced at the surface. Detached eddies would be influenced by entrainment fluxes and by the Coriolis force and, if they are active in the ASL, their statistics would not scale following MOST, which is based on surface parameters. However, we cannot in general preclude conditions where detached eddies could be of some importance. The scaling of the efficiencies

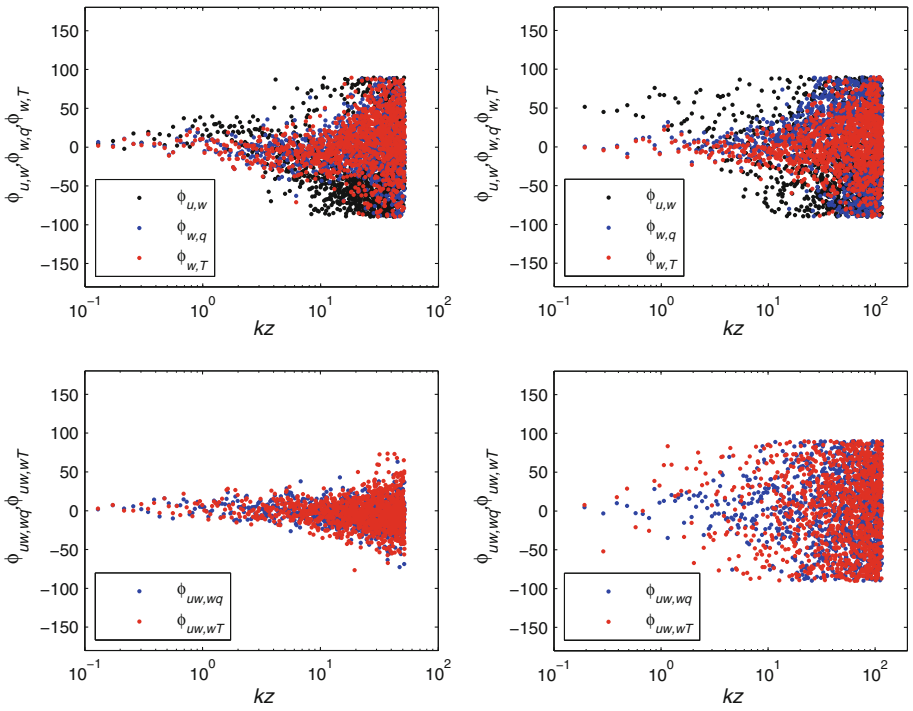

Fig. 5 Spectral analysis of two selected segments (phase spectra). **a** $z/L = -0.1252$ and **b** $z/L = -0.6244$

following MOST has been previously discussed for the correlation coefficients (De Bruin et al. 1993; Choi et al. 2004); fitted MOST functions for the variation of these correlation coefficients with stability are of the form:

$$R_{uw} = \frac{1}{C_{u1}C_{w1}\left(1 - C_{u2}\frac{z}{L}\right)^{\frac{1}{3}}\left(1 - C_{w2}\frac{z}{L}\right)^{\frac{1}{3}}}, \tag{12}$$

$$R_{wq} = R_{wT} = \frac{\left(1 - C_{T2}\frac{z}{L}\right)^{\frac{1}{3}}}{C_{w1}C_{T1}\left(1 - C_{w2}\frac{z}{L}\right)^{\frac{1}{3}}}. \tag{13}$$

Our finding that the quadrant analysis efficiencies follow the same trend is new but not surprising, given that the two efficiencies are related. We observe that the data for the quadrant analysis efficiencies also collapse well when MOST scaling is used. Using the same functional forms used by De Bruin et al. (1993) for the correlation coefficients, we fit a curve through the quadrant analysis efficiencies and compute the fitting coefficients as in Eqs. 12 and 13. Table 2 lists these fitting coefficients for the correlations from De Bruin et al. (1993), from Choi et al. (2004), and from this study. The last column on the other hand lists the fitting coefficients that were obtained for the quadrant analysis efficiencies, assuming that the same functional form of Eqs. 12 and 13 applies to these new efficiencies.

It should be pointed out that, even under close-to-neutral conditions, the transport of momentum and scalars does not seem to be exactly "similar" since the figures suggest that the relative transport efficiencies (R_{uw}/R_{wc} and η_m/η_c, where $c = q, T$) are larger than 1 ($R_{uw}/R_{wc} \approx 1.38$; and $\eta_m/\eta_c \approx 1.10$), implying momentum is transported more efficiently

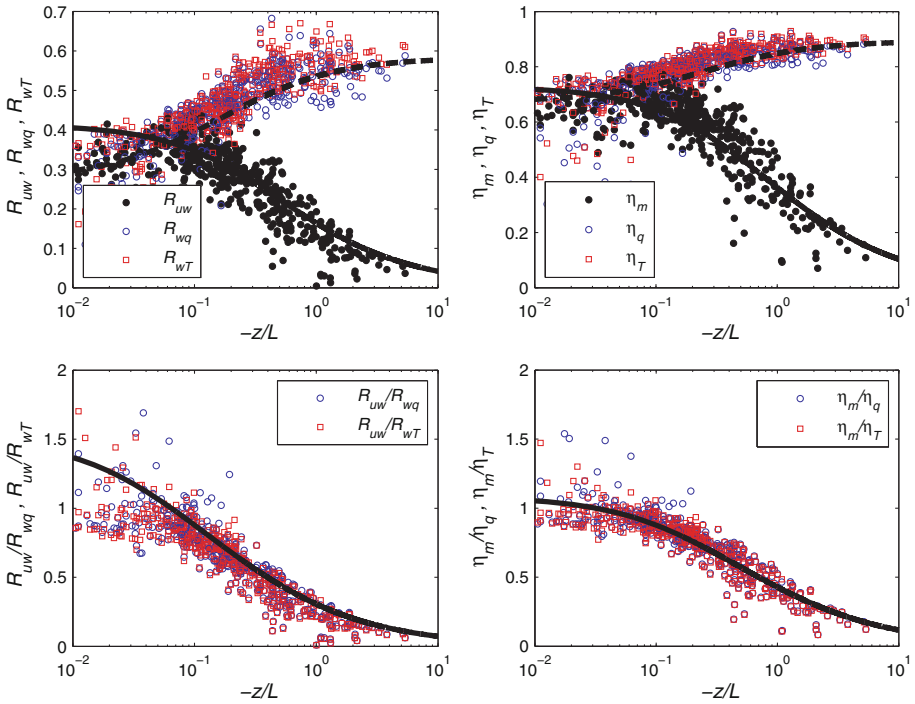

Fig. 6 Transport efficiencies of momentum and scalar fluxes (lake data)

than scalars. We note that these efficiencies are not directly comparable to the efficiencies based on the turbulent diffusivities where it is often observed that the turbulent Prandtl or Schmidt number under neutral conditions is less than one (see, for example, the review in Kays 1994) and hence our results do not contradict these findings. Computation of the turbulent diffusivities was difficult in our study because of the small vertical extent of our set-up and thus the low signal-to-noise ratio when atmospheric gradients were computed. However, we can compute the diffusivities when gradients between the air and surface are used (larger signal). An appropriate way of presenting these diffusivities is to use the bulk transfer coefficients of momentum, heat and moisture:

$$C_m(z) = \frac{u_*^2}{\bar{u}(z)^2}, \tag{14a}$$

$$C_T(z) = \frac{-H}{\rho c_p \bar{u}(z)\,(T(z) - T_s)}, \tag{14b}$$

$$C_q(z) = \frac{-E}{\rho \bar{u}(z)\,(q(z) - q_s)}, \tag{14c}$$

where the subscript s refers to the surface value, and the surface specific humidity is computed as the saturation value at the surface temperature using the polynomial fits provided in Brutsaert (2005). Figure 8 depicts the ratio of these turbulent bulk transfer coefficients for momentum and scalars using the lake data; we note that these ratios are equivalent to the ratios of turbulent diffusivities when the gradients are assumed linear between the surface and height z. Therefore, we also plot in the figure two relevant empirical equations for the

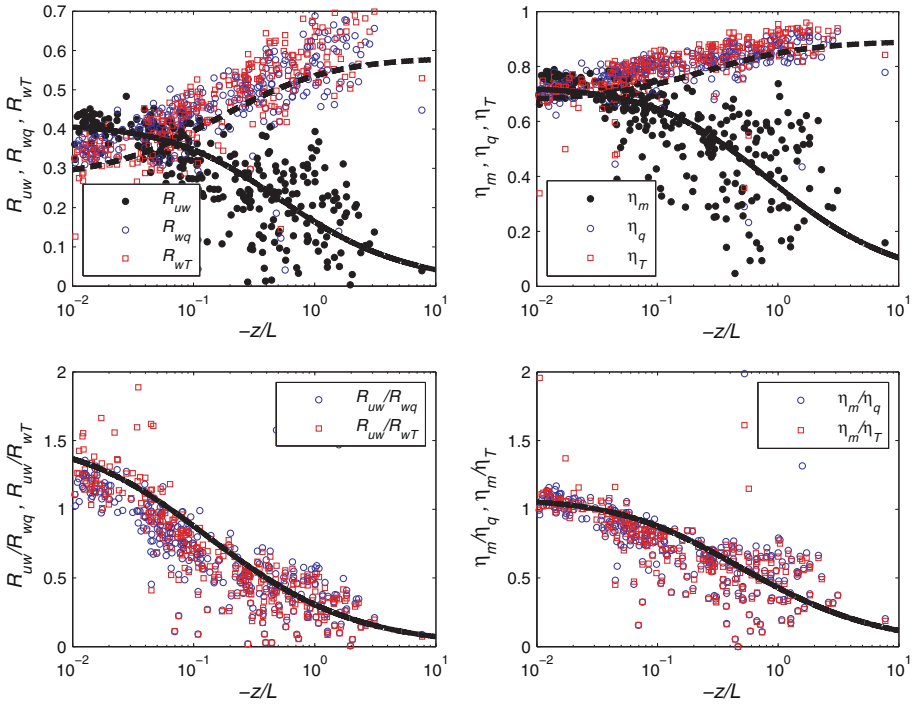

Fig. 7 Transport efficiencies of momentum and scalar fluxes (vineyard data)

Table 2 Monin–Obukhov similarity function coefficients for transport efficiencies

	De Bruin et al. (1993)	Choi et al. (2004)	This study: correlation coefficients	This study: quadrant analysis efficiencies
C_{u1}	2.2	3.13	2.2	1.25
C_{u2}	3	8	3	1
C_{w1}	1.25	1.12	1.1	1.1
C_{w2}	3	2.8	3	3
C_{T1}	2.9	3.7	3.3	1.35
C_{T2}	28.4	34.5	28.4	7

variation of the ratio of turbulent diffusivities with stability. The results again clearly show a decrease in the ratio of momentum to scalar transport efficiency.

An important feature in the dependency of the different efficiencies on stability that should be underlined is that, despite the fact that buoyancy is dominated by both sensible and latent heat fluxes and that these two fluxes have different diurnal cycles over the lake (their 15-min averages are not well correlated, despite the good correlation of their instantaneous values), the decorrelation of the momentum flux with both scalar fluxes is similar. The scalar transport efficiencies are also very similar. This precludes an explanation of the efficiency trends based merely on the ratio of the fluxes (self-correlation of the x-axis and y-axis variables) since low

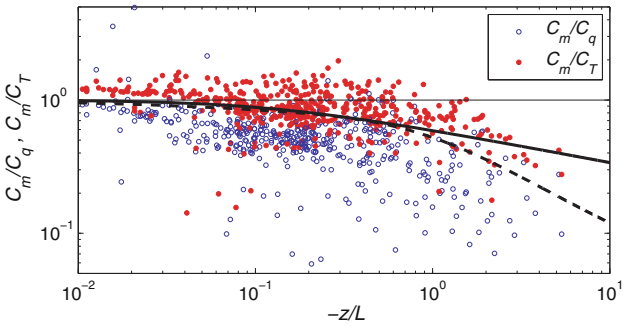

Fig. 8 Ratios of bulk transfer coefficients of momentum and scalars using the lake data; the *black line* is the empirical equation for the ratio of diffusivities from Hogstrom (1988) and the *dashed line* is the equivalent equation from Brutsaert (2005)

sensible heat and moisture fluxes can (separately) occur at high $-z/L$ (humidity contribution to buoyancy is very significant over the lake).

4.3 Atmospheric Stability Effects on Coherent Structures

As discussed in Sect. 4.1, the dissimilarity between the turbulent transport of momentum and scalars arises under unstable conditions. In this section, the characteristics associated with coherent structures in the ABL are analyzed to assess whether they are related to the observed changes in transport efficiency. The starting hypothesis based on the review in the introduction is that coherent structures change from hairpin vortices and packets under close-to-neutral conditions to thermal plumes under convective conditions. If this hypothesis is correct, then we expect to observe the following:

1. a noticeable change in the time-series plots of the different variables with ramp structures being present under unstable conditions due to thermals, as suggested in Stull (1988);
2. a decrease in the horizontal vorticity components with increasing instability since hairpin vortices produce significant streamwise (in the legs) and cross-stream (in the leading edge) vorticity but thermals are mainly expected to produce vertical vorticity though we note that vorticity can certainly be redistributed between components and that hairpins also have significant vertical vorticity (in the legs);
3. a shift in the balance between sweep and ejection fluxes since thermals are expected to perform upward fluxes in short, intense ejections surrounded by weaker longer sweeps, while hairpins produce a complex pattern of a sweep in front of their leading edge and outside of their legs and a long ejection in their core.

First, we examined the time series for ramp structures associated with u, w, q and T and the cross-stream fluctuating vorticity (the only vorticity components we can compute) in two selected 2- min segments, the first under close-to-neutral and the other under strongly unstable conditions. We note that the cross-stream fluctuating vorticity is computed at the upper three sonics using backward finite-differences for vertical gradients (difference between the sonic and the one below it) and by invoking Taylor's hypothesis to compute streamwise gradients, again using finite-differences with a step $\mathrm{d}x = \mathrm{d}z = 0.65$ m, following:

$$\omega_y' = \frac{\partial u'}{\partial z} - \frac{\partial w'}{\partial x}. \tag{15}$$

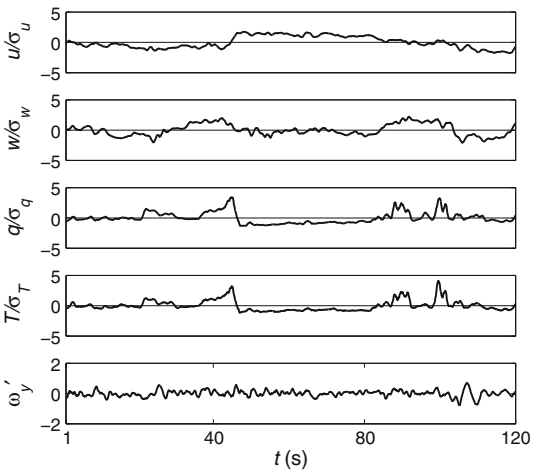

Fig. 9 A selected 2-min interval of u, w, q, T (normalized by their respective root-mean-squares) and ω'_y under unstable conditions: z/L (2 min) $= -0.53$; z/L (15 min) $= -1.00$

The basic characteristics of the two segments are presented in Table 3 for both the 2-min period (statistics may not be converged but are useful to consider) and the 15-min record in which it is located; note that both heat fluxes are considerably higher in the near-neutral record, but the high friction velocity keeps this interval near-neutral. As shown in Fig. 9 (unstable) and Fig. 10 (near-neutral), ramp structures under unstable conditions are different from those under close-to-neutral conditions and consist of gradual rises followed by sudden falls in T and q, which is consistent with previous studies under unstable conditions (e.g. Gao et al. 1989; Paw et al. 1992). The signature of thermals is also visible as regions of strong upward motions (positive w) surrounded by regions of weaker subsidence. On the other hand, the time series for the near-neutral case are less intermittent, and feature shorter and smoother changes. The intermittency difference is clear despite the fact that the spatial extent of the two series is not the same due to a difference in the mean wind speed. One can also note significantly higher magnitudes of the cross-stream fluctuating vorticity under near-neutral conditions, which strongly points to the presence of cross-stream vortices that could be the leading edges of hairpin vortices. However, in the absence of three-dimensional visualization or at least the three vorticity components (which can be computed from other sonic-array configurations), we can only postulate about the exact structure of these eddies. What is very clear from these figures however is that the turbulent structures in near-neutral and convective ASLs have quite different features and these differences agree with the hypothesized change from hairpins to thermals.

The skewnesses of u, w, q and T are shown in Fig. 11. Over the lake surface and under convective conditions, one would expect the skewnesses of w, q and T to be positive because of the influence of the narrow, warm and moist updrafts (Mahrt 1991a). As we can see in Fig. 11, the computed skewnesses of w, q and T are indeed positive and larger under unstable conditions, indicating that positive departures from the mean (updrafts) tend to be stronger than negative departures (downdrafts), which was also observed in Fig. 10. We again note that strong similarity exists between the two scalars, namely, temperature and water vapour, which implies that their transport is controlled by the surface of the lake, which is the source of both, and by surface-layer dynamics, with no noticeable outer flow or advection effects. The skewness of u is expected to be of opposite sign under such convective conditions since updrafts carry lower velocity air and downdrafts carry faster air; surprisingly, this is not the

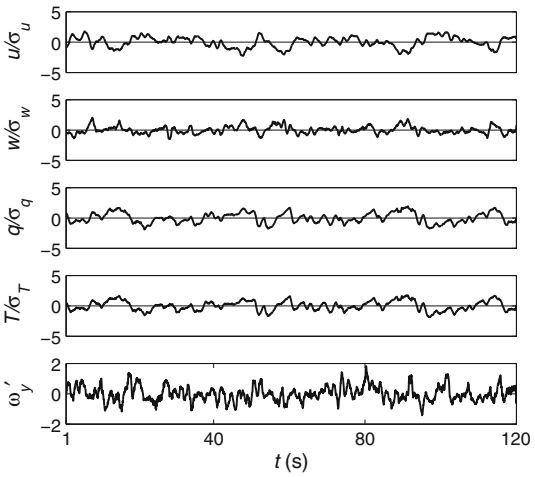

Fig. 10 A selected 2-min interval of u, w, q, T (normalized by their respective root-mean-squares) and ω'_y under close to neutral conditions z/L (2 min) $= -0.02$; z/L (15 min) $= -0.02$

Table 3 Characteristics of the two selected segments (Figs. 9, 10)

	Averaging time (min)	Unstable	Near-neutral
u (m s^{-1})	2	1.41	10.64
	15	1.79	10.95
T (K)	2	286.54	288.31
	15	286.58	288.83
q (kg m^{-3})	2	0.011	0.012
	15	0.011	0.011
z/L	2	−0.54	−0.02
	15	−1.00	−0.02
u_* (m s^{-1})	2	0.11	0.64
	15	0.10	0.60
H (W m^{-2})	2	13.93	61.77
	15	20.32	77.56
LE (W m^{-2})	2	36.34	255.94
	15	60.83	258.47

case and the skewness of u does not change significantly with stability. This suggests that buoyancy-produced thermals significantly alter the distributions of w, q and T but hardly alter the distribution of u; consequently, streamwise momentum transport due to thermals is very weak and inefficient. This confirms the trends in Figs. 9 and 10 and illustrates the lower correlation of u and w under unstable conditions, which explains the lower momentum transport efficiency discussed in Sect. 4.2.

As mentioned before, hairpin vortices and packets are expected to result in higher cross-stream vorticity. Therefore, a decrease in the fluctuating cross-stream vorticity would provide additional evidence that this transition does actually occur in the ASL. The r.m.s. of the fluctuating vorticity is depicted in Fig. 12, which illustrates the expected decrease of the cross-stream vorticity as instability increases, confirming the observation from the two short records. The values level off when z/L exceeds -0.5, which confirms that coherent

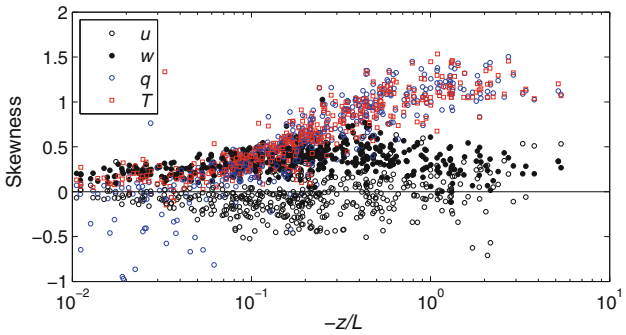

Fig. 11 Skewness of u, w, q and T

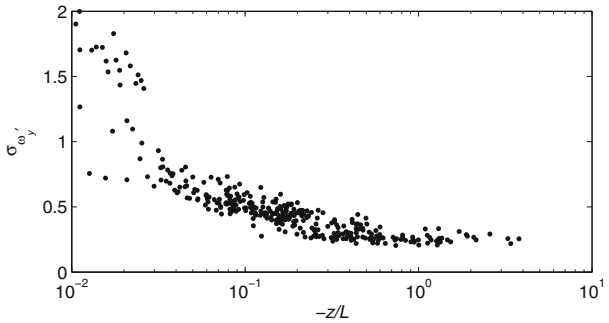

Fig. 12 Root-mean-square of the cross-stream fluctuating vorticity

structures experience a transition from structures with strong horizontal vorticity to vertical updrafts as instability increases. This would also suggest that hairpin vortices are not likely to be observed when $z/L < -0.5$. One thing to be noted is that when we use the r.m.s. of the cross-stream fluctuating vorticity, the mean velocity gradient effect is removed. The decrease of this quantity is hence necessarily related to the change of turbulence structure and/or intensity rather than to the decrease in the mean shear.

In this section, where we are focusing on turbulence structure, we have thus far illustrated how increasing instability changes the structure of turbulence in a manner that is very consistent with the expected shift from hairpin vortices to thermal plumes, but the link to fluxes and their efficiency has not yet been established, although the different skewness trends already suggest such a link. Since these fluxes are performed by ejections and sweeps, we will next investigate how the ejection–sweep cycle is modified by atmospheric stability. We compute the differences in the flux contribution fraction ΔS and time fraction ΔD of ejection and sweep events, which illustrate the relative importance of ejection and sweep events in terms of flux contribution and the time fraction occupied by such events, respectively. These differences are given by

$$\Delta S = S_{\text{ejections}} - S_{\text{sweeps}}, \tag{16}$$

$$\Delta D = D_{\text{ejections}} - D_{\text{sweeps}}. \tag{17}$$

The results are presented in Fig. 13. Under near-neutral conditions, ejection and sweep events are of the same significance while as instability increases and thermals become the main transporting structure, flux contributions from ejection events become increasingly larger

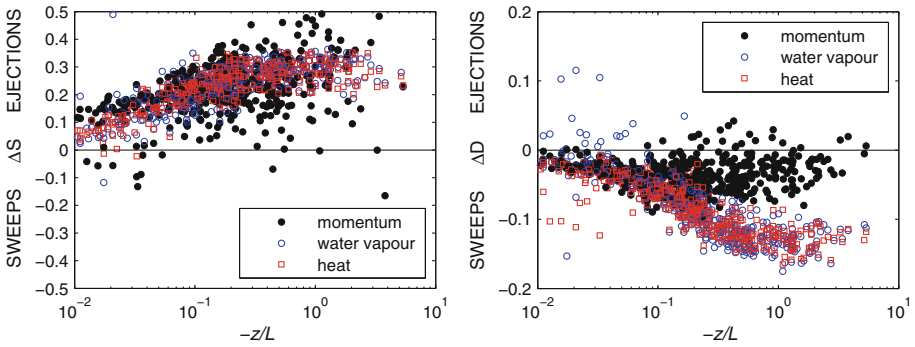

Fig. 13 The relative importance of ejection and sweep events in terms of flux contribution and time fraction: (*left*) flux contribution and (*right*) time fraction

than sweep events for both momentum and scalar fluxes. This increase in the role of ejections was shown to be linked to an increase in the vertical flux transport terms (mainly $\overline{w'w'u'}$ and $\overline{w'u'u'}$) by Katul et al. (1997a,b). Thus, the effect of unstable conditions on the fluxes seems to stem mainly from increased vertical transport of $\overline{w'u'}$and $\overline{u'u'}$ by thermals and the resulting effect these transport terms have on the fluxes.

Note that the behaviour of ΔS is almost the same for the momentum flux and for the scalar fluxes, although for momentum the scatter is noticeably higher. This might suggest that the result is similar transport under all conditions, contradicting the previous findings. However, this similarity does not hold when the time fraction ΔD is considered. For scalar fluxes, the time fraction of sweep events becomes increasingly larger than that of ejection events as instability increases while for momentum flux, it seems the difference between the time fractions of ejections and sweeps increase at first and then decrease to zero. Figure 13 illustrates the fact that the stronger ejection events (thermals/updrafts) contribute more to the fluxes, but occupy less time than sweep events for scalars, which suggests higher transport efficiencies for scalars under unstable conditions. These ejections also dominate the downgradient transport of momentum but the phase lag and decorrelation of u and w under unstable conditions result in differences with scalar transport: while ejections dominate the downgradient momentum flux under unstable conditions, their time fraction does not decrease as with scalars. Results (not shown here) indicate that, in fact, the time fraction of all events (sweeps, ejections, and outward and inward interactions), as well as the average flux per event, for momentum become almost equal under unstable conditions. Thus, the increased countergradient transport of momentum by inward and outward interactions under unstable conditions, resulting from the phase lag between u and w and illustrated by the decrease in momentum transport efficiency based on the quadrant analysis (Figs. 6, 7), is the main cause of the decrease in momentum transport efficiency with increasing instability.

5 Conclusions

Atmospheric stability effects on the turbulent transport of momentum and scalars (temperature and water vapour) are investigated, with a specific focus on the link between the change in coherent structure topology and transport dissimilarity. It is observed that the correlations between the momentum flux and scalar fluxes decrease as the atmosphere changes from neutral to unstable. Under near-neutral conditions, coherence and phase spectra indicate that the transports of momentum and scalars are synchronized (performed by the same updrafts

and downdrafts) and well correlated. Under unstable conditions, this similarity breaks down and the motions transporting momentum and scalars become distinct or unsynchronized. The systematic phase difference between momentum and scalar fluxes under unstable conditions, which is related to the structure and dynamics of the vertical plumes and potentially to the effects of pressure (Mahrt 1991b), confirms this dissimilarity. Different measures of transport efficiencies (correlation coefficients, transport efficiencies based on quadrant analysis, and bulk transfer coefficients) are analyzed and confirm the increasing dissimilarity of momentum and scalar transport under unstable conditions, with scalars becoming more efficiently and momentum drastically less efficiently transported as buoyancy increases. These efficiencies are further found to obey Monin–Obukhov similarity relations that we propose and test in this study.

Starting with the hypothesis that coherent structures change from hairpin vortices and packets under close-to-neutral conditions to thermal plumes under convective conditions, we proceed to analyze the effect of stability on the topology of turbulent coherent structures and the links to transport efficiency. Ramp structures, ejections and sweeps, and the fluctuating vorticity of coherent structures are analyzed and the results agree with our hypothesis. We observe that ramp structures are strongly modified by stability, with longer and more intermittent events under unstable conditions. The ejection–sweep cycle is also dependent on atmospheric stability and ejections are found to become more efficient than sweeps in producing turbulent fluxes as instability increases (more intense updrafts and slower, weaker downdrafts). The results also confirm that, under neutral conditions, coherent structures have strong cross-stream vorticity that would be expected with hairpin vortices. As instability sets in, a change of these structures into thermal plumes is observed. The transition of coherent structures from eddies with significant horizontal vorticity to larger thermal plumes is suggested as the cause of the dissimilarity between the transport of momentum and scalars.

The results obtained from two field experimental datasets collected over very different surfaces prove that the dissimilarity between the turbulent transport of momentum and scalar fluxes, and its sensitivity to stability, are consistent over a wide range of surface types. While the evidence presented here about the role of buoyancy in modulating coherent structures and the link of this topological change to transport efficiency is strong and goes beyond visualizations of individual events as reported in previous studies, three-dimensional velocity and scalar data are needed in the future to look at the details of these effects and to answer further questions such as the following: Are the neutral-ASL eddies mainly or exclusively hairpin vortices and packets? Is there a gradual or abrupt shift from hairpins to thermals as buoyancy flux increases? At intermediate stabilities, do we have intermediate structures that have features of both, or do we observe distinct hairpins and thermals alternating in the ASL?

Acknowledgments The authors would like to thank the team of the Environmental Fluid Mechanics and Hydrology Laboratory at the Swiss Federal Institute of Technology—Lausanne, especially Professor Marc Parlange and Dr. Hendrik Huwald, where co-author Bou-Zeid worked during the two experiments described here, for the collection of the datasets. The authors are also grateful to the High Meadows Foundation (through the Princeton Sustainability Initiative) and for the Mid-Infrared Center For Health and the Environment at Princeton University for their support.

References

Adrian RJ (2007) Hairpin vortex organization in wall turbulence. Phys Fluids 19(4):041301

Asanuma J, Tamagawa I, Ishikawa H, Ma YM, Hayashi T, Qi YQ, Wang JM (2007) Spectral similarity between scalars at very low frequencies in the unstable atmospheric surface layer over the Tibetan plateau. Boundary-Layer Meteorol 122:85–103

Assouline S, Tyler SW, Tanny J, Cohen S, Bou-Zeid E, Parlange MB, Katul GG (2008) Evaporation from three water bodies of different sizes and climates: measurements and scaling analysis. Adv Water Resour 31:160–172

Boppe RS, Neu WL, Shuai H (1999) Large-scale motions in the marine atmospheric surface layer. Boundary-Layer Meteorol 92:165–183

Bou-Zeid E, Vercauteren N, Parlange MB, Meneveau C (2008) Scale dependence of subgrid-scale model coefficients: an a priori study. Phys Fluids 20:115106

Bou-Zeid E, Higgins C, Huwald H, Meneveau C, Parlange MB (2010) Field study of the dynamics and modelling of subgrid-scale turbulence in a stable atmospheric surface layer over a glacier. J Fluid Mech 665:480–515

Brutsaert W (2005) Hydrology: an introduction. Cambridge University Press, New York, 605 pp

Carper MA, Porte-Agel F (2004) The role of coherent structures in subfilter-scale dissipation of turbulence measured in the atmospheric surface layer. J Turbul 5:040

Cava D, Katul GG, Sempreviva AM, Giostra U, Scrimieri A (2008) On the anomalous behaviour of scalar flux-variance similarity functions within the canopy sub-layer of a dense alpine forest. Boundary-Layer Meteorol 128:33–57

Choi TJ, Hong JK, Kim J, Lee HC, Asanuma J, Ishikawa H, Tsukamoto O, Gao ZQ, Ma YM, Ueno K, Wang JM, Koike T, Yasunari T (2004) Turbulent exchange of heat, water vapor, and momentum over a Tibetan prairie by eddy covariance and flux variance measurements. J Geophys Res-Atmos 109:D21106

De Bruin HAR, Kohsiek W, Vandenhurk BJJM (1993) A verification of some methods to determine the fluxes of momentum, sensible heat, and water-vapor using standard-deviation and structure parameter of scalar meteorological quantities. Boundary-Layer Meteorol 63:231–257

De Bruin HAR, VanDen Hurk B, Kroon LJM (1999) On the temperature–humidity correlation and similarity. Boundary-Layer Meteorol 93:453–468

Detto M, Katul G, Mancini M, Montaldo N, Albertson JD (2008) Surface heterogeneity and its signature in higher-order scalar similarity relationships. Agric For Meteorol 148:902–916

Drobinski P, Carlotti P, Newson RK, Banta RM, Foster RC, Redelsperger JL (2004) The structure of the near-neutral atmospheric surface layer. J Atmos Sci 61:699–714

Drobinski P, Carlotti P, Redelsperger JL, Banta RM, Masson V, Newsom RK (2007) Numerical and experimental investigation of the neutral atmospheric surface layer. J Atmos Sci 64:137–156

Etling D, Brown RA (1993) Roll vortices in the planetary boundary-layer—a review. Boundary-Layer Meteorol 65:215–248

Gao W, Shaw RH, Paw KT (1989) Observation of organized structure in turbulent-flow within and above a forest canopy. Boundary-Layer Meteorol 47:349–377

Head MR, Bandyopadhyay P (1981) New aspects of turbulent boundary-layer structure. J Fluid Mech 107:297–338

Hogstrom U (1988) Non-dimensional wind and temperature profiles in the atmospheric surface-layer—a re-evaluation. Boundary-Layer Meteorol 42:55–78

Hogstrom U, Hunt JCR, Smedman AS (2002) Theory and measurements for turbulence spectra and variances in the atmospheric neutral surface layer. Boundary-Layer Meteorol 103:101–124

Hommema SE, Adrian RJ (2003) Packet structure of surface eddies in the atmospheric boundary layer. Boundary-Layer Meteorol 106:147–170

Horiguchi M, Hayashi T, Hashiguchi H, Ito Y, Ueda H (2010) Observations of coherent turbulence structures in the near-neutral atmospheric boundary layer. Boundary-Layer Meteorol 136:25–44

Huang J, Cassiani M, Albertson JD (2009) Analysis of coherent structures within the atmospheric boundary layer. Boundary-Layer Meteorol 131:147–171

Hunt JCR, Carlotti P (2001) Statistical structure at the wall of the high Reynolds number turbulent boundary layer. Flow Turbul Combust 66:453–475

Hunt JCR, Morrison JF (2000) Eddy structure in turbulent boundary layers. Eur J Mech B 19:673–694

Hutchins N, Marusic I (2007) Evidence of very long meandering features in the logarithmic region of turbulent boundary layers. J Fluid Mech 579:1–28

Inagaki A, Kanda M (2010) Organized structure of active turbulence over an array of cubes within the logarithmic layer of atmospheric flow. Boundary-Layer Meteorol 135:209–228

Kanda M (2006) Large-eddy simulations on the effects of surface geometry of building arrays on turbulent organized structures. Boundary-Layer Meteorol 118:151–168

Katul G, Hsieh CI, Kuhn G, Ellsworth D, Nie DL (1997a) Turbulent eddy motion at the forest–atmosphere interface. J Geophys Res-Atmos 102:13409–13421

Katul G, Kuhn G, Schieldge J, Hsieh CI (1997b) The ejection–sweep character of scalar fluxes in the unstable surface layer. Boundary-Layer Meteorol 83:1–26

Katul GG, Sempreviva AM, Cava D (2008) The temperature–humidity covariance in the marine surface layer: a one-dimensional analytical model. Boundary-Layer Meteorol 126:263–278
Kays WM (1994) Turbulent Prandtl number—where are we. J Heat Transf 116:284–295
Kays WM, Crawford ME, Weigand B (2005) Convective heat and mass transfer. McGraw-Hill Higher Education, Boston
Kim KC, Adrian RJ (1999) Very large-scale motion in the outer layer. Phys Fluids 11:417–422
Kline SJ, Reynolds WC, Schraub FA, Runstadl PW (1967) Structure of turbulent boundary layers. J Fluid Mech 30:741–773
Lee X, Yu Q, Sun X, Liu J, Min Q, Liu Y, Zhang X (2004) Micrometeorological fluxes under the influence of regional and local advection: a revisit. Agric For Meteorol 122:111–124
Mahrt L (1991a) Boundary-layer moisture regimes. Q J Roy Meteorol Soc 117:151–176
Mahrt L (1991b) Eddy asymmetry in the sheared heated boundary-layer. J Atmos Sci 48:472–492
Marusic I, Mathis R, Hutchins N (2010a) Predictive model for wall-bounded turbulent flow. Science 329: 193–196
Marusic I, McKeon BJ, Monkewitz PA, Nagib HM, Smits AJ, Sreenivasan KR (2010b) Wallbounded turbulent flows at high Reynolds numbers: Recent advances and key issues. Phys Fluids 22(6):065103
Mason PJ, Sykes RI (1980) A two-dimensional numerical study of horizontal roll vortices in the neutral atmospheric boundary-layer. Q J Roy Meteorol Soc 106:351–366
Mason PJ, Sykes RI (1982) A two-dimensional numerical study of horizontal roll vortices in an inversion capped planetary boundary layer. Q J Roy Meteorol Soc 108:801–823
McNaughton KG, Brunet Y (2002) Townsend's hypothesis, coherent structures and Monin–Obukhov similarity. Boundary-Layer Meteorol 102:161–175
McNaughton KG, Laubach J (1998) Unsteadiness as a cause of non-equality of eddy diffusivities for heat and vapour at the base of an advective inversion. Boundary-Layer Meteorol 88:479–504
Moene AF, Schuttemeyer D (2008) The effect of surface heterogeneity on the temperature–humidity correlation and the relative transport efficiency. Boundary-Layer Meteorol 129:99–113
Monty JP, Stewart JA, Williams RC, Chong MS (2007) Large-scale features in turbulent pipe and channel flows. J Fluid Mech 589:147–156
Moriwaki R, Kanda M (2006) Local and global similarity in turbulent transfer of heat, water vapour, and CO2 in the dynamic convective sublayer over a suburban area. Boundary-Layer Meteorol 120:163–179
Paw KT, Brunet Y, Collineau S, Shaw RH, Maitani T, Qiu J, Hipps L (1992) On coherent structures in turbulence above and within agricultural plant canopies. Agric For Meteorol 61:55–68
Ringuette MJ, Wu MW, Martin MP (2008) Coherent structures in direct numerical simulation of turbulent boundary layers at Mach 3. J Fluid Mech 594:59–69
Robinson SK (1991) Coherent motions in the turbulent boundary-layer. Annu Rev Fluid Mech 23:601–639
Schmidt H, Schumann U (1989) Coherent structure of the convective boundary-layer derived from large-eddy simulations. J Fluid Mech 200:511–562
Sempreviva AM, Gryning SE (2000) Mixing height over water and its role on the correlation between temperature and humidity fluctuations in the unstable surface layer. Boundary-Layer Meteorol 97:273–291
Sempreviva AM, Hojstrup J (1998) Transport of temperature and humidity variance and covariance in the marine surface layer. Boundary-Layer Meteorol 87:233–253
Shaw RH, Tavangar J, Ward DP (1983) Structure of the Reynolds stress in a canopy layer. J Clim Appl Meteorol 22:1922–1931
Smedman AS, Hogstrom U, Hunt JCR, Sahlee E (2007) Heat/mass transfer in the slightly unstable atmospheric surface layer. Q J Roy Meteorol Soc 133:37–51
Stull RB (1988) An introduction to boundary layer meteorology. Kluwer, Dordrecht, 670 pp
Theodorsen T (1952) Mechanism of turbulence. In: Second Midwestern conference on fluid mechanics. Ohio State University, Columbus, OH
Vercauteren N, Bou-Zeid E, Parlange MB, Lemmin U, Huwald H, Selker J, Meneveau C (2008) Subgrid-scale dynamics of water vapour heat, and momentum over a lake. Boundary-Layer Meteorol 128:205–228
Williams CA, Scanlon TM, Albertson JD (2007) Influence of surface heterogeneity on scalar dissimilarity in the roughness sublayer. Boundary-Layer Meteorol 122:149–165
Wyngaard JC (1985) Structure of the planetary boundary-layer and implications for its modeling. J Clim Appl Meteorol 24:1131–1142
Wyngaard JC, Moeng CH (1992) Parameterizing turbulent-diffusion through the joint probability density. Boundary-Layer Meteorol 60:1–13